The Astrophysical Journal, 857:36 (7pp), 2018 April 10 https://doi.org/10.3847/1538-4357/aab714

Impact of Shock Front Rippling and Self-reformation on the Electron Dynamics at Low-Mach-number Shocks

Zhongwei Yang[1,2], Quanming Lu[2], Ying D. Liu[1,3], and Rui Wang[1,4]
[1] State Key Laboratory of Space Weather, National Space Science Center, Chinese Academy of Sciences, Beijing 100190, People's Republic of China; liuxying@swl.ac.cn
[2] CAS Key Laboratory of Geospace Environment, Chinese Academy of Sciences, Department of Geophysics and Planetary Science, University of Science and Technology of China, Hefei 230026, People's Republic of China; qmlu@ustc.edu.cn
[3] University of Chinese Academy of Sciences, Beijing 100049, People's Republic of China
[4] W. W. Hansen Experimental Physics Laboratory, Stanford University, Stanford, CA 94305, USA
Received 2017 December 1; revised 2018 March 11; accepted 2018 March 13; published 2018 April 11

Abstract

Electron dynamics at low-Mach-number collisionless shocks are investigated by using two-dimensional electromagnetic particle-in-cell simulations with various shock normal angles. We found: (1) The reflected ions and incident electrons at the shock front provide an effective mechanism for the quasi-electrostatic wave generation due to the charge-separation. A fraction of incident electrons can be effectively trapped and accelerated at the leading edge of the shock foot. (2) At quasi-perpendicular shocks, the electron trapping and reflection is nonuniform due to the shock rippling along the shock surface and is more likely to take place at some locations accompanied by intense reflected ion-beams. The electron trapping process has a periodical evolution over time due to the shock front self-reformation, which is controlled by ion dynamics. Thus, this is a cross-scale coupling phenomenon. (3) At quasi-parallel shocks, reflected ions can travel far back upstream. Consequently, quasi-electrostatic waves can be excited in the shock transition and the foreshock region. The electron trajectory analysis shows these waves can trap electrons at the foot region and reflect a fraction of them far back upstream. Simulation runs in this paper indicate that the micro-turbulence at the shock foot can provide a possible scenario for producing the reflected electron beam, which is a basic condition for the type II radio burst emission at low-Mach-number interplanetary shocks driven by Coronal Mass Ejections (CMEs).

Key words: acceleration of particles – shock waves – Sun: heliosphere

1. Introduction

Collisionless shocks are of great interest in space physics, plasma physics, and astrophysics. In the shock transition, the bulk energy of the plasma is converted into thermal energy in the absence of particle collisions (Tidman & Krall 1971; Lembège et al. 2004; Burgess et al. 2005). Collisionless shocks provide us with good opportunities to explore nonlinear dynamics in strongly inhomogeneous and nonstationary plasma discontinuities (Hada et al. 2003; Matsukiyo & Scholer 2003; Yang et al. 2009; Hao et al. 2017). For high-Mach-number shocks, two-dimensional (2D) particle-in-cell (PIC) simulation results show that a fraction of incident electrons can be reflected at the leading edge of the shock foot (Matsumoto et al. 2013, 2015). Extreme circumstances encountered in such situations can be realized in astrophysical phenomena (Kato & Takabe 2010), such as supernova remnant shocks (Wieland et al. 2016). However, the electron trapping and reflection at low-Mach-number shocks is still unclear.

The interplanetary shock (IP) database developed and maintained at University of Helsinki (http://ipshocks.fi) shows that most of IP shocks (from 1975 January 06 to 2017 May 27) have Mach numbers less than 7. Furthermore, Richardson & Cane (2010) found that if a trailing CME-driven shock penetrates into a leading CME, it can have an even lower Mach number (Lugaz et al. 2015). Such situations correspond to low-Mach-number shocks in collisionless space plasmas, in contrast to very-high-Mach-number astrophysical shocks. The striking point to note here is that we do observe type II ratio bursts emitted at CME-driven shocks (e.g., Bale et al. 1999; Liu et al. 2009; Krupar et al. 2016). It is generally believed that the origin of such type II bursts is associated with reflected electron beams at CME-driven shocks (e.g., Bale et al. 1999). The electron trapping and shock surfing acceleration mechanism was first discussed by Shimada & Hoshino (2000). They found that a fraction of incident electrons can be reflected by the bipolar electric field structure in the shock transition at high-Mach-number shocks (Hoshino & Shimada 2002), and the bipolar electrostatic structure has been observed by the *Wind* spacecraft (Bale et al. 1998). At low-Alfvénic-Mach-number ($\sim$4.4) shocks, early one-dimensional (1D) PIC simulations indicate that no reflected electrons can be found (Sugiyama et al. 2003). Later 2D PIC simulations reveal that the low-Mach-number shock in the supercritical regime can be nonstationary (Lembège et al. 2009; Umeda et al. 2009; Matsukiyo & Matsumoto 2015). There are two dominant mechanisms for explaining the nonstationarity of moderate- or low-Mach-number shocks: (1) shock front self-reformation (which can be observed even at 1D PIC simulations), and (2) shock front ripples (which are at least 2D phenomena). The impact of shock front nonstationarity on the electron dynamics at low-Mach-number shocks is a particularly interesting issue.

Bohdan et al. (2017) studied the electron pre-acceleration at high-Mach-number, strictly perpendicular astrophysical shocks, and they found that the electrostatic potential wells at the foot are important for the electron reflection and trapping. They perform different runs for strictly perpendicular shocks with different ambient magnetic field orientations. In their simulations, ambient B is perpendicular to the flow direction (i.e., the X-direction) and lies in the yz plane, forming an angle ϕ with the y-axis. They concluded that for a strictly out-of-plane field or the so-called

Table 1
Upstream Conditions of Simulation Runs and Derived Shock Properties

Run	θ_{Bn}(°)	$(\omega_{pe}/\Omega_{ce})^2$	c/v_A	m_i/m_e	β_i	β_e	$v_{\rm inj}/v_A$	M_A
1	90	400	90	20	0.01	0.3	4	5.5
2	30	400	90	20	0.01	0.3	4	5.2

Note. θ_{Bn} is the shock normal angle between directions of the ambient magnetic field and the shock normal; the ratio of ω_{pe} and Ω_{ce} reveals the magnetization of the upstream plasmas.

Bo – OUT case in previous PIC simulations (Lembège et al. 2009; Yang et al. 2012), the fraction of superthermal electrons is much higher than for other configuration, because only in this case are the Buneman modes fully captured by the 2D simulation. However, the electron trapping and acceleration at low-Mach-number quasi-parallel shocks has not yet been investigated. We expect that our work in this paper on different shocks with different shock normal angles θ_{Bn} may give us a preliminary understanding of the electron dynamics at perpendicular and quasi-parallel shocks in the low-Mach-number regime.

The paper is organized as follows. We present a description of the simulation model and setup in Section 2. The results are presented in Section 3, and we conclude with a discussion and summary in Section 4.

2. Simulation Model

We carry out 2D PIC simulations using EPOCH PIC code (Arber et al. 2015) with a normalization the same as that used in Yang et al. (2015, 2016) to simulate the micro-structures of low-Mach-number, supercritical shocks. In this paper, a shock wave was created by the so-called injection method, in which particles are injected from one side of the simulation boundary (here, $x = 0$) at super-Alfvénic speed $V_0 = 4V_{\rm A}$ in the $+x$-direction and specularly reflected at the other side of the simulation boundary ($x = L_x$), as in previous simulations (Burgess et al. 1989; Matsukiyo & Scholer 2012; Yang et al. 2015). The shock propagates in the $-x$-direction in the present downstream rest frame. A periodic boundary condition is used in the y-direction. We adopted simulation parameters of the ion-to-electron mass ratio of $m_i/m_e = 20$, and the upstream magnetization $(\omega_{pe}/\Omega_{ce})^2 = 400$. The upstream magnetic field has the x- and y-components. Two different shock normal angles, $\theta_{Bn} = 90°$ and $\theta_{Bn} = 30°$, are used for simulations of perpendicular (Run 1) and quasi-parallel (Run 2) shocks, respectively. Setups of these runs are shown in Table 1. The number of grid cells is $n_x \times n_y = 11{,}000 \times 2100$. The electron inertial length d_e resolved with 50 computational cells, and one numerical time step resolves $0.0135\omega_{pe}^{-1}$, where ω_{pe} is the electron plasma frequency in the upstream region. Fifty particles per cell per species were used in the upstream region. In total, more than one billion particles were followed in the simulation domain.

3. Simulation Results

The low-Mach-number shocks studied in this paper are nonstationary and evolve with time. Figures 1(a), (b) show the time-evolution of y-averaged shock main magnetic field $\overline{B}_y$ and shock normal electric field $\overline{E}_x$ profiles. These figure panels shows that the shock front is undergoing self-reformation (Matsukiyo & Scholer 2003; Yang et al. 2009). Plots similar to Figure 1(b) for time-evolving local E_x at two different locations ($Y = 3.55d_i$ and $Y = 5.74d_i$) along the shock surface are showed in Figures 1(c), (d), respectively. In 2D shock simulations, the shock front micro-turbulence and particle behaviors are mainly modulated by two mechanisms: (1) the shock front rippling and (2) the shock front self-reformation. A zoomed view of the foot region is plotted in the insets of Figures 1(c), (d). They indicate that a wave that has a large shock normal electric field component E_x can be excited at the leading edge of the foot. The strongest amplitude of the wave appears at different self-reformation cycles for different shock profiles selected at different locations along the rippling shock surface.

First, we investigate the characteristics of the wave excited at the shock foot. For example, the shock profile A is chosen at a fixed time $t = 3.6\Omega_{ci}^{-1}$, which is marked by "A" in Figure 1(c). Figure 2(a) shows the ion bulk velocity (zoomed in) at this shock profile. The red color represents the incident solar wind ions with a positive bulk speed V_{ix}, and the blue region indicates the region of high-intensity reflected ions. The charge-separation of ions and electrons $dQ = Q_i - Q_e$ (Figure 2(b)) is obvious in the strong ion reflection region. Figures 2(b), (c) show that the sign and amplitude of dQ match well with the shock normal electric field component E_x of the excited wave at the leading edge of the foot. The magnetic field component (Figure 2(d)) of the wave is very weak relative to the electric field component in this case. The wave could possibly be classified as a quasi-electrostatic wave.

Second, we investigate the impact of the shock front self-reformation (Lembège & Savoini 1992; Hada et al. 2003) on the wave excitation and electron dynamics. Shock profiles A and B (marked by dashed lines in Figure 1(c)) are chosen at a fixed location ($Y = 3.55d_i$) along the shock surface at two typical times ($t = 3.6\Omega_{ci}^{-1}$ and $t = 4.7\Omega_{ci}^{-1}$) within one self-reformation cycle. For profile A (Figure 3), Figure 3(a) (the main magnetic field B_y) shows that the shock front is in a narrow and steep phase during the self-reformation. In Figure 3(b), the shock normal electric field E_x shows that large amplitude quasi-electrostatic waves are excited at the leading edge of the foot (around $X = 43d_i$). Corresponding local phase space plots (X–V_{ix}) of ions are shown in Figure 3(c). Ions are continuously injected from the left-hand side, and a large number of them are reflected at the ramp (at about $X = 44d_i$). This phenomenon is consistent with that observed in previous 1D hybrid and PIC simulations (Burgess et al. 1989; Yang et al. 2009). The local magnetic field (red curve) and shock normal electric field (white curve) are also shown for reference in arbitrary units. Figure 3(d) shows the corresponding phase space plot (X–V_{ex}) of electrons. The foot region has been zoomed in and plotted in the inset. It shows that a fraction of incident electrons are strongly modulated and trapped by the quasi-electrostatic waves, which have many bipolar structures as observed by the *Wind* spacecraft (Bale et al. 1998).

Figure 4 is the same as Figure 3 but for profile B at $t = 4.7\Omega_{ci}^{-1}$. For the comparison, the same color bar scale is used in Figures 3 and 4. In profile B, the shock front is in a wide and flat phase during the self-reformation. Figure 4(a) shows that the new shock front grows up at about $X = 41.5d_i$. In contrast to the profile A, Figure 4(b) shows that there is no quasi-electrostatic wave at the wide foot. In Figure 3(c), the

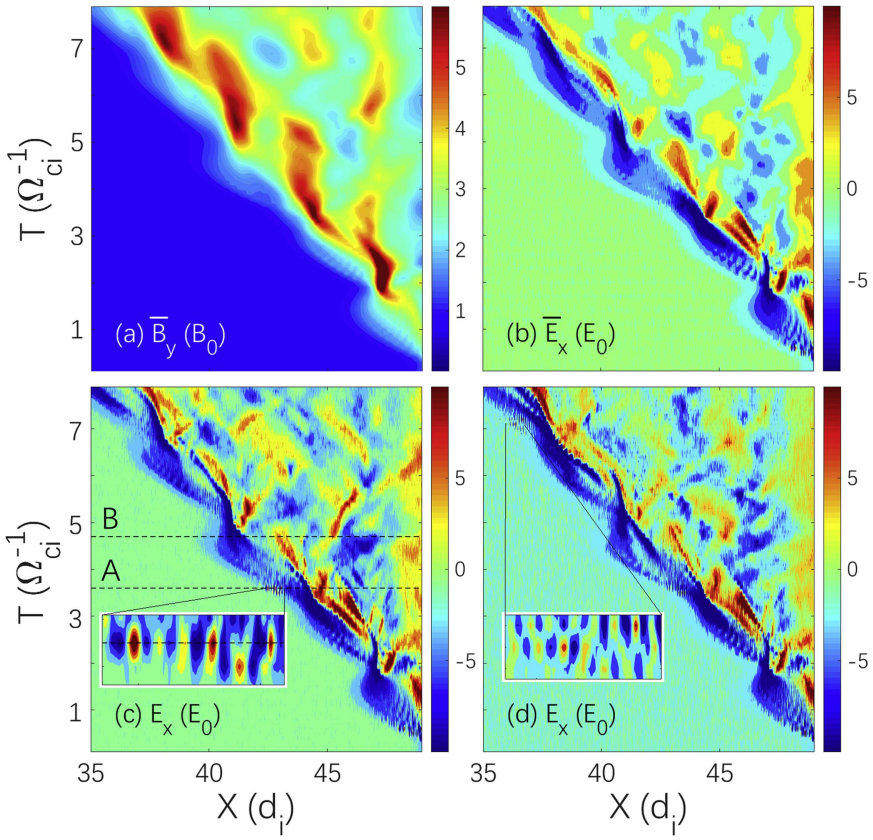

Figure 1. Stackplots of nonstationary perpendicular shock profiles in Run 1. (a) y-averaged main magnetic field component B_y. (b) y-averaged shock normal electric field component E_x. (c) Different local E_x profiles sampled at different locations along the y-direction: (c) $Y = 3.55d_i$ and (d) $Y = 5.74d_i$, respectively. Details of the shock foot quasi-electrostatic wave are zoomed in and plotted in the insets. In panel (c), two shock profiles at different times within one self-reformation cycle are marked by "A" ($t = 3.6\Omega_{ci}^{-1}$) and "B" ($t = 4.7\Omega_{ci}^{-1}$), respectively.

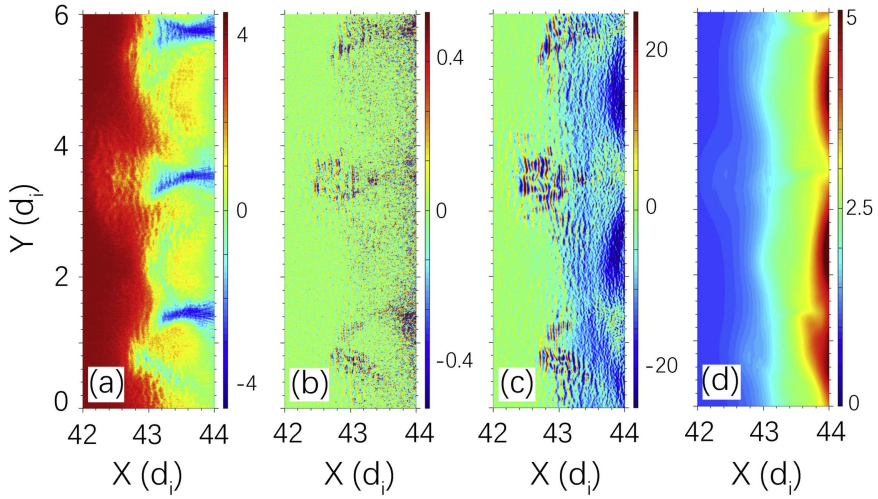

Figure 2. Shock profile A ($t = 3.6\Omega_{ci}^{-1}$) has been chosen to describe the characteristic of waves excited at the foot region. (a) Bulk speed V_{ix} of ions around the foot region. (c) Charge-separation between ions and electrons $dQ = Q_i - Q_e$. (d) Electric field component E_x along the shock normal. (e) Strength of the total magnetic field B. The magnetic fields are normalized by the upstream field B_0, and the electric fields are normalized by $v_A B_0$.

intensity of reflected ions at the new shock front is very weak because the new ramp is not fully grown. Most of the incident ions are directly transmitted. In Figure 4(d), there is no trapping electron. In summery, the shock front self-reformation caused by the ion reflection can modulate the quasi-electrostatic wave and the electron dynamics. At a steep and narrow shock profile, waves can be excited and their amplitudes become large. A lot of electrons are trapped by these waves at the leading edge of the foot. In contrast, at a flat and wide shock profile, the quasi-electrostatic wave cannot be excited. As a result, incident electrons cannot be trapped during their shock crossing.

Third, we investigate the impact of the shock front rippling (Savoini & Lembège 1994; Burgess et al. 2016) on the wave excitation and electron dynamics. As discussed above, if the shock profile is relatively steep and narrow, then the quasi-electrostatic wave and electron trapping can take place. Thus,

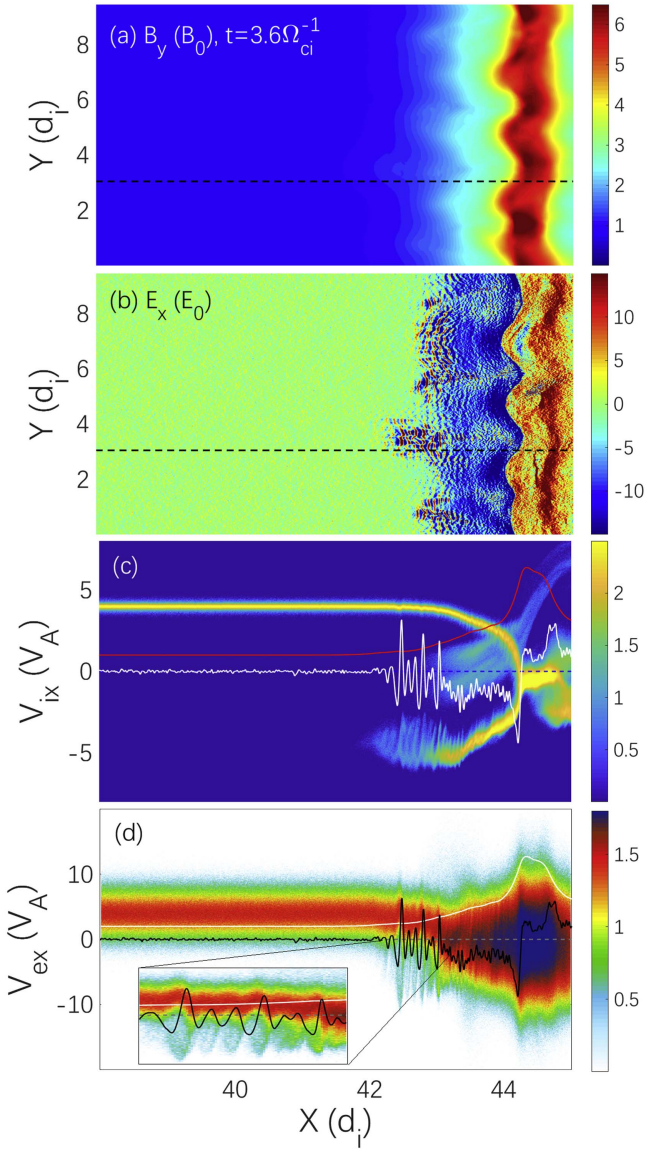

Figure 3. Snapshot of the shock profile A in Run 1 at $t = 3.6\Omega_{ci}^{-1}$: the steep and narrow shock front phase within one self-reformation cycle (marked by "A" in Figure 1(c)). (a) The main magnetic field component B_y. (b) The shock normal electric field E_x. (c) The phase space plot (X–V_{ix}) of ions at a fixed location ($Y = 3.55d_i$), which is marked by a black dashed line in panels (a) and (b). Local B_y (red) and E_x (white) are shown for reference in arbitrary units. (d) Same as plots in panel (c) for electrons. Local B_y (white) and E_x (black) are shown for reference in arbitrary units. The electron trapping region has been zoomed in and plotted in a subgraph.

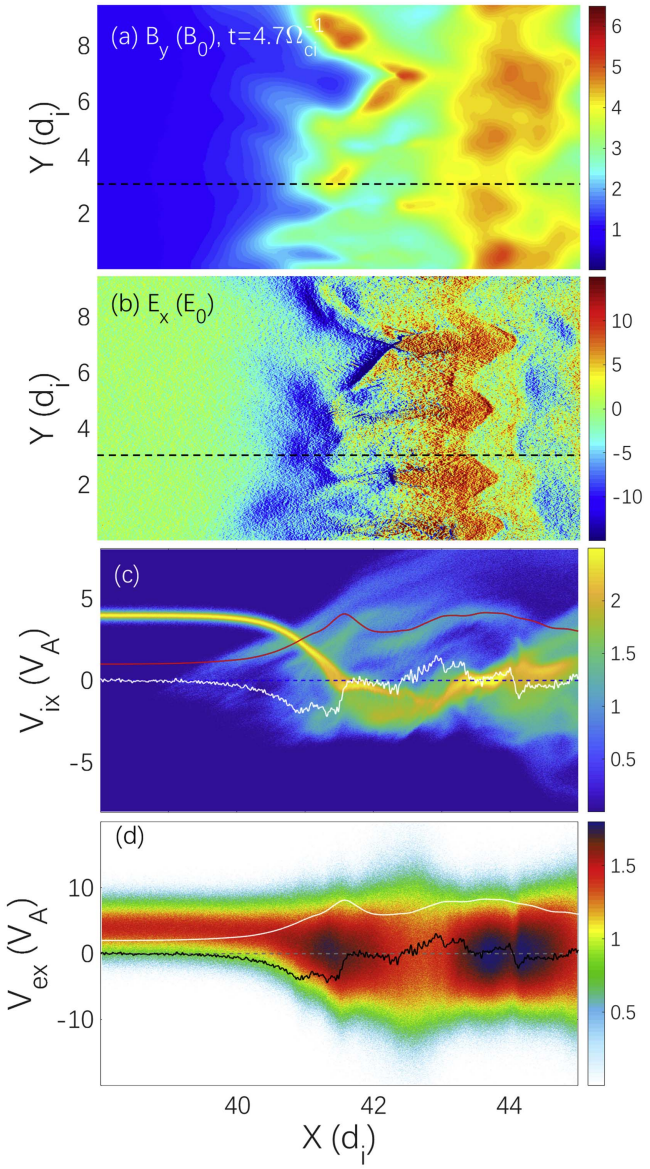

Figure 4. Same as Figure 2 but for the shock profile B at $t = 4.7\Omega_{ci}^{-1}$, the flat and wide shock front phase within the same self-reformation cycle (marked by "B" in Figure 1(c)).

the shock profile at the fixed time $t = 3.6\Omega_{ci}^{-1}$ is selected to study the influence of shock rippling. Two local shock profiles ("C" and "D," marked by arrows in Figure 5(a)) are chosen at different locations ($Y = 3.35d_i$ and $Y = 2.18d_i$) along the shock surface. At profile C (Figures 5(b), (d)), strong waves and trapping electrons are found, as expected. At profile D (Figure 5(c)), the intensity of the reflected ions at the foot region (around $X = 43.5d_i$) decreased from yellow to green compared with that in profile C in Figure 5(b) (the same color bar is used). Therefore, Figure 5(e) shows that no quasi-electrostatic waves or newly trapped electrons can be found at the leading edge of the foot. Therefore, both the shock front self-reformation and the shock front rippling can affect the excitation of the quasi-electrostatic wave and the electron trapping. Even if the shock profile is steep, the intensity of reflected ions can be very weak in places, and it is inhomogeneous along the shock surface because of the shock front ripples. Only at the location associated with strong reflection can ion intensity lead to wave generation and the resulting electron trapping.

Moreover, the energization capability of the shock foot quasi-electrostatic wave to the electrons is investigated. The trapping electrons are traced from upstream to downstream. In Figure 6(a) ($t = 3.5\Omega_{ci}^{-1}$), the traced electrons are trapped by the quasi-electrostatic wave at the shock foot. At a later time ($t = 3.7\Omega_{ci}^{-1}$, Figure 6(b)), they are trapped for a while at the shock ramp. Simultaneously, they become diffusive along the local B field. In Figure 6(c) ($t = 4.5\Omega_{ci}^{-1}$), the old ramp becomes weak, and the foot grows up and finally evolves into a new ramp. At this time, the traced electrons penetrate the shock ramp and approach the immediate downstream region. Finally ($t = 4.9\Omega_{ci}^{-1}$, Figure 6(d)), traced electrons undergo drift

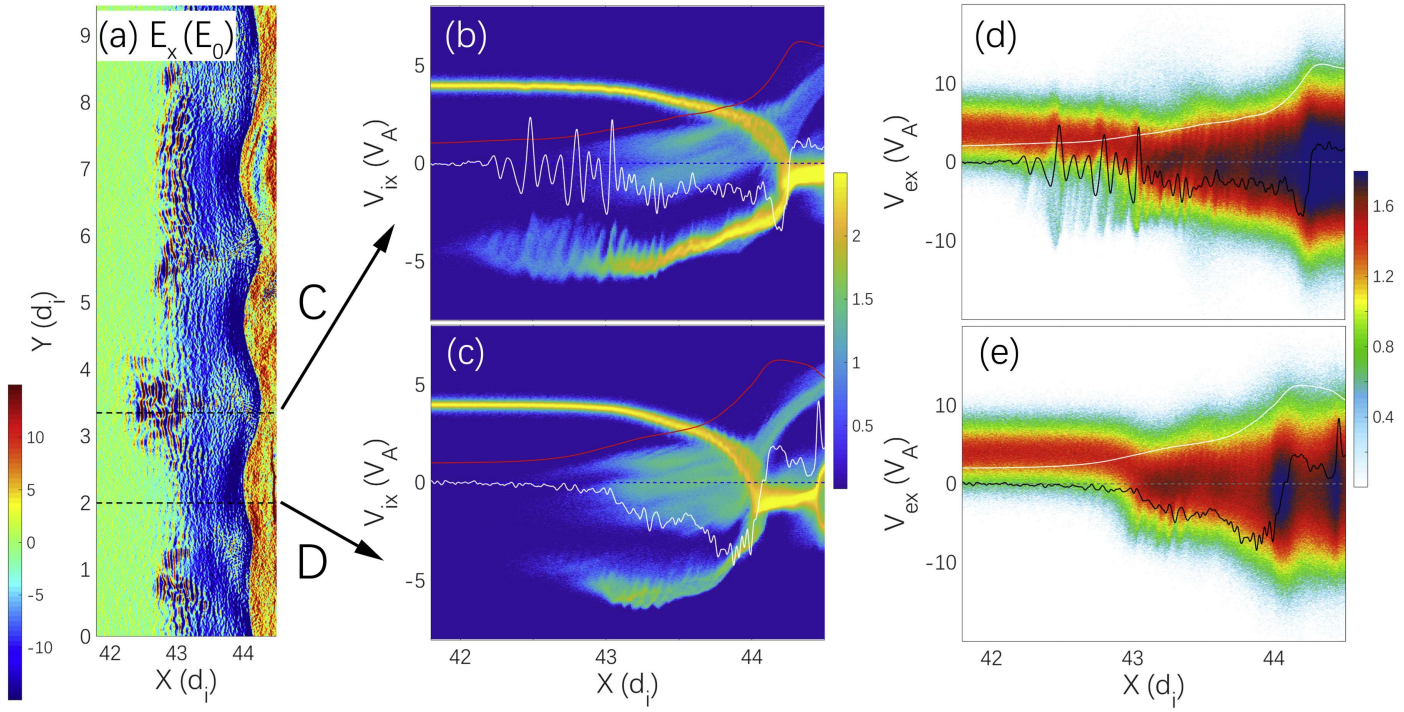

Figure 5. (a) Snapshot of the shock profile A in Run 1 at $t = 3.6\Omega_{ci}^{-1}$: impact of the shock front ripples. Two shock profiles "C" and "D" are chosen along the rippling shock surface at $Y = 3.35d_i$ and $Y = 2.18d_i$, respectively. (b, c) Phase space plots (X–V_{ix}) of ions as in Figure 2 for shock profiles C and D, respectively. (d, e) Corresponding phase space plots (X–V_{ex}) of electrons.

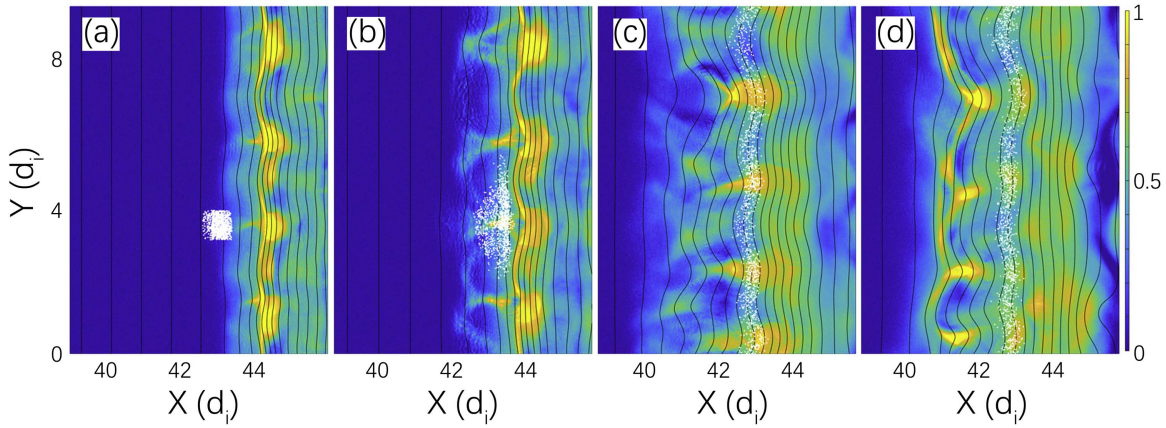

Figure 6. Trapping and accelerated electrons (white dots) are traced from upstream to downstream and are plotted at different times $t = 3.5$, 3.7, 4.5, and $4.9\Omega_{ci}^{-1}$ in panels (a–d), respectively. The background contours depict the electron density profile N_e. To improve visualization, one-tenth of traced electrons are plotted, and magnetic field lines are also shown for reference.

motion and are convected far downstream. In Figure 7, the time-evolution of energy spectra is calculated for these traced electrons during the whole shock crossing process (from $t = 3.5\Omega_{ci}^{-1}$ to $t = 4.9\Omega_{ci}^{-1}$, the time interval is $0.1\Omega_{ci}^{-1}$). Different colors indicate the energy spectrum calculated at different times. Blue shows the spectrum obtained at the beginning, and the red curve indicates the final state. The time-evolution of energy spectra shows that electrons are mainly heated before $t = 4\Omega_{ci}^{-1}$ when they are being trapped in the foot and ramp regions. When they penetrate the downstream region, their energy spectrum has no big change.

Finally, to investigate the impact of the shock normal angle θ_{Bn} on the ES wave, we carried out a quasi-parallel shock case (Run 2 in Table 1), and the results are shown in Figure 8. Figures 8(a), (b) show the phase space plots of ions and electrons at $t = 4.8\Omega_{ci}^{-1}$. In contrast to the quasi-perpendicular case, many reflected ions and electrons can travel far back upstream due to the orientation of the ambient magnetic field. Figures 8(c), (d) show the shock normal electric field E_x and the total magnetic field B_y of the quasi-parallel shock. Two typical trajectories of electrons are traced during their shock crossing (Figure 8(e)). The electric field profile E_x is also showed for reference. The light blue curve indicates a transmitted electron (marked by "B"), which penetrates the shock without any large scale reflection (relative to the small scale trapping at about $X = 42d_i$). The red curve indicates a reflected electron (marked by "A"), which is trapped by the excited quasi-electrostatic wave at the foot region ($39d_i < X < 43d_i$) and is then reflected far back upstream ($X < 39d_i$). This shows there is a large difference between perpendicular shocks and quasi-parallel

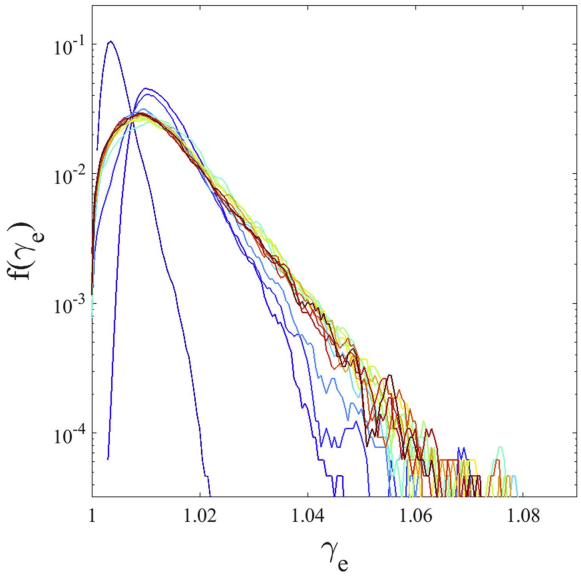

Figure 7. Time-evolution of energy spectra $f(\gamma_e)$ for the traced electrons during the shock crossing. They are calculated from $t = 3.5\Omega_{ci}^{-1}$ to $t = 4.9\Omega_{ci}^{-1}$ (in colors from cold to warm), where γ_e is the Lorentz factor. The time interval of the calculations is $0.1\Omega_{ci}^{-1}$.

shocks. The time-evolving pitch angle of the electron "A" is represented in Figure 8(f). The pitch angle distribution of all electrons at $t = 4.8\Omega_{ci}^{-1}$ is plotted as the background (colors indicate the particle count in a log scale). There is evidence that some incident electrons are reflected at the shock ramp ($X \sim 44d_i$) and their pitch angles are gathered to ~90°. This is a typical characteristic of the magnetic mirror, as suggested by Wu (1984) (a Fast Fermi-type reflection). Moreover, a fraction of incident electrons can be trapped by the quasi-electrostatic field E_x at the foot region and undergo a strong pitch angle scatter (around $X = 38, 40, 42d_i$, etc.). This process can also generate reflected electrons. Compared with the former, this process is more random and similar to that mentioned by Matsukiyo & Scholer (2012, shock front micro-turbulence reflection).

4. Conclusion and Discussion

In this paper, we have used a full particle kinetic simulation to study the electron reflection at low-Mach-number shocks. By probing results in detail through a variety of diagnostic techniques, we have shown the following properties:

1. At a low-Mach-number shock, a fraction of the incident ions can be reflected by the shock. The interaction of reflected ions and the incoming electrons can excite quasi-electrostatic waves at the shock foot.
2. In contrast to the ions that are mainly reflected at the shock ramp, the electrons are almost trapped and reflected at the leading edge of the foot. Because the B field is very weak there and the electric field along the shock normal is very strong, the adiabatic condition of some incident electrons could be broken. The electrons can be accelerated during their trapping process within the shock transition and form a non-thermal tail in their energy spectrum.
3. At quasi-perpendicular shocks, the shock front self-reformation caused by the intermittent ion reflection can modulate the quasi-electrostatic wave and the electron dynamics. Both wave excitation and electron trapping are in favor of a steep and narrow shock that is accompanied by intense reflected ions.
4. At quasi-perpendicular shocks, the shock front rippling caused by the inhomogeneous ion reflection can also

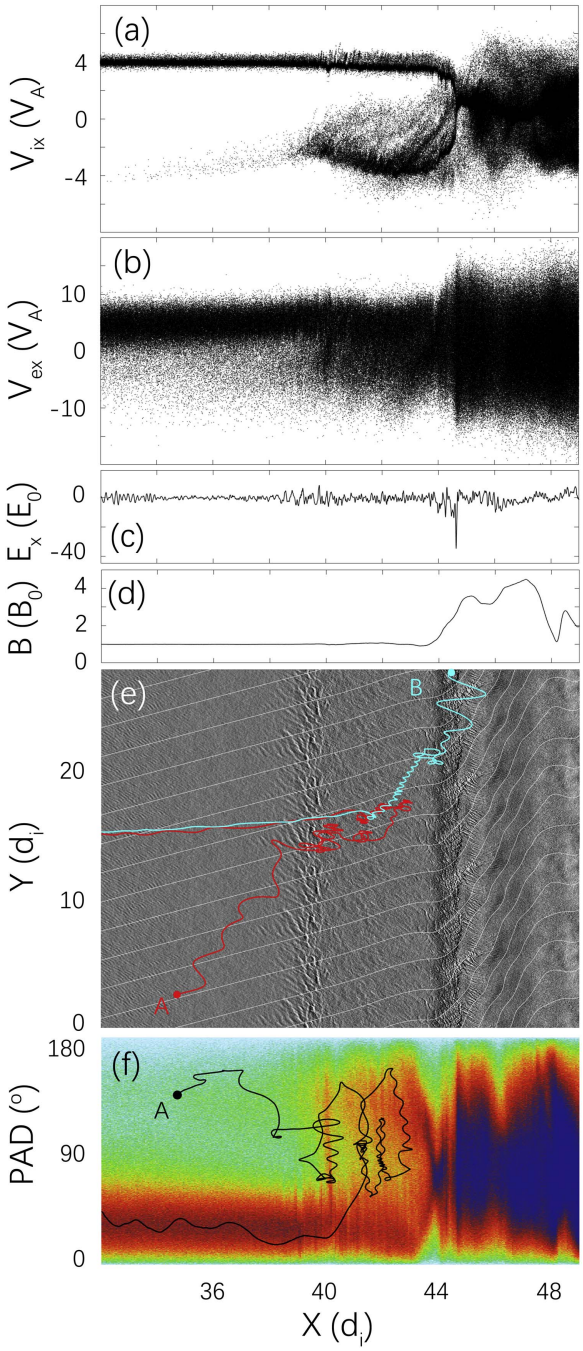

Figure 8. (a, b) Phase space plots (X–V_{ix}) of ions and electrons, respectively. (c, d) Shock normal electric field E_x and total magnetic field B_y at the quasi-parallel shock ($\theta_{Bn} = 30°$) at $t = 4.8\Omega_{ci}^{-1}$. (e) Trajectories of two typical electrons: light blue and red curves indicate a transmitted electron ("B") and a reflected electron (trapped at the foot and escaped far upstream, marked by "A"). Note that the background shock E_x profile (a snapshot at $t = 4.8\Omega_{ci}^{-1}$) is extended in the y-direction (periodic boundaries are used in the simulation for the y-direction) in order to intuitively show the full trajectory of electrons. (f) Pitch angle distribution (PAD) of all electrons (the background contour) at $t = 4.8\Omega_{ci}^{-1}$. Color represents the count of electrons in a log scale. The black curve indicates the time-evolving pitch angle of the traced particle "A."

modulate the quasi-electrostatic wave and the electron dynamics. The wave excitation and the electron trapping are in favor of specific areas in the presence of intense reflected ions.

5. At quasi-parallel shocks, the quasi-electrostatic wave also can be excited at the foot region. In addition, the trapped electrons can be reflected far back upstream. It is quite different from the very local trapping process at quasi-perpendicular shocks.

The quasi-electrostatic wave has implications for the linear instability theory of modes (electron cyclotron drift instability, ion-acoustic instability, modified two-stream instability, Buneman instability) expected within the shock transition (Matsukiyo & Scholer 2003; Matsumoto et al. 2012; Umeda et al. 2012; Muschietti & Lembège 2013), which will be investigated in later work. In this paper, our results mainly focus on the capability of low-Mach-number interplanetary (IP) shocks (refer to the IP shock parameters for the observations around 1 au, e.g., http://usuarios.geofisica.unam.mx/primoz/IPShocks.html, and http://ipshocks.fi/database) on the electron trapping, reflection, acceleration, and heating. The primary goal is to illustrate that a rippling and reforming shock can produce energetic reflected electrons that are possible candidates for the generation mechanism of the type II radio burst, as observed by Bale et al. (1999). In summary, the electron trapping and reflection can take place not only in the very-high-Mach-number astrophysical shocks but also in low-Mach-number IP CME-driven shocks. Based on the local Alfvén speed model (e.g., Vainio et al. 2003) and CME speed measured by STEREO (e.g., Liu et al. 2013, 2014; Hu et al. 2016) from the Sun to about 200 solar radii, the CME-driven shock Mach number can be roughly estimated as a function of distance. Although such a Mach number would not be as high as astrophysical shocks, it is high enough to generate reflected electrons in the foreshock and trigger the type II ratio burst emission. Both the background solar wind turbulence (e.g., Guo & Giacalone 2010) and the compressed heliospheric current sheets inside the sheath region of the CME-driven shock (e.g., Zank et al. 2015) also need to be considered in future work.

The authors are grateful to Christopher Brady, Shuichi Matsukiyo, and Can Huang for helpful discussions on numerical techniques. The research was supported by NFSC under grant Nos. 41574140, 41374173, and 41604146, the Recruitment Program of Global Experts of China, the Specialized Research Fund for State Key Laboratories of China, the Open Research Program Key laboratory of Geospace Environment CAS (GE2017-01). The supercomputer resources are partially supported by Youth Innovation Promotion Association funding (2017188), Strategic Priority Program on Space Science (XDA15011300), and Beijing Excellent Talent Training Project Funding (2017000097607G049).

ORCID iDs

Zhongwei Yang https://orcid.org/0000-0002-1509-1529
Quanming Lu https://orcid.org/0000-0003-3041-2682
Ying D. Liu https://orcid.org/0000-0002-3483-5909

References

Arber, T. D., Bennett, K., Brady, C. S., et al. 2015, PPCF, 57, 113001
Bale, S. D., Kellogg, P. J., Larsen, D. E., et al. 1998, GeoRL, 25, 2929
Bale, S. D., Reiner, M. J., Bougeret, J.-L., et al. 1999, GeoRL, 26, 1573
Bohdan, A., Niemiec, J., Kobzar, O., & Pohl, M. 2017, ApJ, 847, 71
Burgess, D., Hellinger, P., Gingell, I., & Trávníček, P. M. 2016, JPlPh, 82, 905820401
Burgess, D., Lucek, E. A., Scholer, M., et al. 2005, SSRv, 118, 205
Burgess, D., Wilkinson, W. P., & Schwartz, S. J. 1989, JGR, 94, 8783
Guo, F., & Giacalone, J. 2010, ApJ, 715, 406
Hada, T., Oonishi, M., Lembège, B., & Savoini, P. 2003, JGR, 108, 1233
Hao, Y., Gao, X., Lu, Q., et al. 2017, JGR, 122, 6385
Hoshino, M., & Shimada, N. 2002, ApJ, 572, 880
Hu, H., Liu, Y. D., Wang, R., Möstl, C., & Yang, Z. 2016, ApJ, 829, 97
Kato, T. N., & Takabe, H. 2010, ApJ, 721, 828
Krupar, V., Eastwood, J. P., Kruparova, O., et al. 2016, ApJL, 823, L5
Lembège, B., Giacalone, J., Scholer, M., et al. 2004, SSRv, 110, 161
Lembège, B., & Savoini, P. 1992, PhFlB, 4, 3533
Lembège, B., Savoini, P., Hellinger, P., & Trávníček, P. M. 2009, JGR, 114, A03217
Liu, Y., Luhmann, J. G., Bale, S. D., & Lin, R. P. 2009, ApJL, 691, L151
Liu, Y. D., Luhmann, J. G., Kajdič, P., et al. 2014, NatCo, 5, 3481
Liu, Y. D., Luhmann, J. G., Lugaz, N., et al. 2013, ApJ, 769, 45
Lugaz, N., Farrugia, C. J., Smith, C. W., & Paulson, K. 2015, JGR, 120, 2409
Matsukiyo, S., & Matsumoto, Y. 2015, JPhCS, 642, 012017
Matsukiyo, S., & Scholer, M. 2003, JGR, 108, 1459
Matsukiyo, S., & Scholer, M. 2012, JGR, 117, A11105
Matsumoto, Y., Amano, T., & Hoshino, M. 2012, ApJ, 755, 109
Matsumoto, Y., Amano, T., & Hoshino, M. 2013, PhRvL, 111, 215003
Matsumoto, Y., Amano, T., Kato, T. N., & Hoshino, M. 2015, Sci, 347, 974
Muschietti, L., & Lembège, B. 2013, JGR, 118, 2267
Richardson, I. G., & Cane, H. V. 2010, JGR, 115, A07103
Savoini, P., & Lembège, B. 1994, JGR, 99, 6609
Shimada, N., & Hoshino, M. 2000, ApJ, 543, L67
Sugiyama, T., Matsumoto, H., Omura, Y., & Fujimoto, M. 2003, ICRC, 6, 3693
Tidman, D. A., & Krall, N. A. 1971, Shock Waves in Collisionless Plasmas (New York: Wiley-Interscience)
Umeda, T., Kidani, Y., Matsukiyo, S., & Yamazaki, R. 2012, JGR, 117, A03206
Umeda, T., Yamao, M., & Yamazaki, R. 2009, ApJ, 695, 574
Vainio, R., Laitinen, T., & Fichtner, H. 2003, A&A, 407, 713
Wieland, V., Pohl, M., Niemiec, J., Rafighi, I., & Nishikawa, K.-I. 2016, ApJ, 820, 62
Wu, C. S. 1984, JGR, 89, 8857
Yang, Z., Huang, C., Liu, Y. D., et al. 2016, ApJS, 225, 13
Yang, Z., Liu, Y. D., Richardson, J. D., et al. 2015, ApJ, 809, 28
Yang, Z. W., Lembège, B., & Lu, Q. M. 2012, JGR, 117, A07222
Yang, Z. W., Lu, Q. M., Lembège, B., & Wang, S. 2009, JGR, 114, A03111
Zank, G. P., Hunana, P., Mostafavi, P., et al. 2015, ApJ, 814, 137